Journal of Physics G: Nuclear and Particle Physics

PAPER

Evidence of a slight nuclear transparency in the alpha-nucleus systems

To cite this article: L C Chamon *et al* 2015 *J. Phys. G: Nucl. Part. Phys.* **42** 055102

View the article online for updates and enhancements.

You may also like

- Predictions on the -cluster structure in ^{104}Te
  M A Souza, H Miyake, T Borello-Lewin et al.
- A new simple model for the -decay
  O Bayrak
- Two-delta shell resonance description of -decay: analytic expression of half-life via energy derivative of phase-shift
  Basudeb Sahu

This content was downloaded from IP address 143.107.135.170 on 09/03/2022 at 23:00

IOP Publishing Journal of Physics G: Nuclear and Particle Physics

J. Phys. G: Nucl. Part. Phys. **42** (2015) 055102 (27pp) doi:10.1088/0954-3899/42/5/055102

Evidence of a slight nuclear transparency in the alpha-nucleus systems

L C Chamon[1], **L R Gasques**[1], **G P A Nobre**[2], **E S Rossi Jr**[1,3], **R J deBoer**[4], **C Seymour**[4], **M Wiescher**[4] **and G G Kiss**[5]

[1] Departamento de Física Nuclear, Instituto de Física da Universidade de São Paulo, Caixa Postal 66318, 05315-970, São Paulo, SP, Brazil
[2] National Nuclear Data Center, Brookhaven National Laboratory, Upton, NY 11973-5000, USA
[3] Centro Universitário FIEO—UNIFIEO, Osasco, SP, Brazil
[4] Department of Physics, University of Notre Dame, Notre Dame, IN 46556, USA
[5] Institute of Nuclear Research (ATOMKI), H-4001, Debrecen, Hungary

E-mail: lchamon@if.usp.br

Received 10 December 2014, revised 19 January 2015
Accepted for publication 21 January 2015
Published 19 February 2015

Abstract

In earlier works, we proposed a model for the nuclear potential of the $\alpha + \alpha$ and $\alpha + {}^{12}$C systems. This theoretical model successfully described data related to the elastic and inelastic scattering processes as well as resonances that correspond to the capture reaction channel. In the present work, we extend the same model to obtain bare nuclear potentials for several α-nucleus systems. We adopt this interaction to analyze fusion, elastic, and inelastic scattering data within the context of the coupled-channel formalism. Our results indicate that, for these systems, the absorption of flux of the elastic channel at internal distances of interaction is not complete. In addition, we present new experimental angular distributions for the 2^+ inelastic target excitation of α on ^{120,130}Te.

Keywords: nuclear reactions, elastic scattering, optical models

(Some figures may appear in colour only in the online journal)

1. Introduction

The optical potential (OP) is a fundamental component of nuclear reactions theory. Several models have been developed to describe the OP, mostly for its real part, such as the proximity potential [1, 2], the double-folding (DF) of Satchler and Love [3], the variety of density- and energy-dependent interactions (e.g. [4, 5]), the parameter-free São Paulo potential (SPP) [6],

© 2015 IOP Publishing Ltd Printed in the UK

etc. Apart from a few more fundamental theoretical models (e.g. [7–9]), the imaginary part of the OP is usually treated within some phenomenological approach, mainly when the purpose is for data analysis. In this context, several systematics have been proposed for the OP parameter values (see e.g. [10–12] for nucleon–nucleus, alpha-nucleus and heavy-ion systems).

The coupled-channel (CC) formalism (see e.g. [13]) is often assumed to describe the nuclear reactions. In this approach, a few states from the set of direct channels are included in the coupled equations. The effect of all the remaining states and channels, which, in principle, can be simulated by a complex local-equivalent polarization potential, should be entangled in the real and imaginary parts of the OP. Nevertheless, the polarization potential presents a complex structure, with strong energy and angular momentum dependence, and with a quite complicated shape (see e.g. [14]). Even so, most data analyzes found in the literature have been performed with imaginary potentials that do not exhibit the angular momentum dependence, and assume a simple shape to describe them such as the Woods–Saxon function. On the other hand, when all the important states of the direct channels are explicitly considered in the coupled equations, the respective polarization can be neglected. In this case, the imaginary part of the OP must simulate only the absorption of flux by the fusion process, while the real part can essentially be associated to the bare nuclear force between the nuclei.

Alpha-nucleus scattering has been extensively studied (e.g. [11, 15, 16]). The low-lying states of ^{4}He present high excitation energies and this nucleus has a large binding energy in comparison with its neighboring nuclei. For these reasons, the α particle is almost inert in a nuclear collision. This characteristic makes the scattering of systems involving ^{4}He as a projectile particularly interesting. In fact, due to the small number of reaction channels, for these systems the imaginary part of the OP should play a minor role and, therefore, the study of the real part can be performed much more accurately than with heavy-ion systems. A clear example of this behavior corresponds to the $\alpha + \alpha$ system. In this case, for bombarding energies below 34.6 MeV, the only open reaction channel is ^{4}He(^{4}He,γ)^{8}Be which has a very small cross section. Thus, the elastic scattering is the only relevant channel in this energy range, and the corresponding OP must have a vanishing imaginary part. Based on this important feature, in [17] we proposed a model for the real part of the OP in the case of $\alpha + \alpha$. The theoretical results obtained with this model are in good agreement with the phase-shifts obtained from elastic scattering data analyzes. Also the s-wave resonance of ^{8}Be is reproduced by our model. In a recent paper [14], we applied the same model to the $\alpha + {}^{12}$C system. Again, due to the lack of significant reaction cross sections at low energies, the imaginary part of the OP for this system was assumed to be perturbative. In this case, however, our calculations were performed within the CC formalism, considering the coupling between the elastic and the ^{12}C 2^{+} inelastic channels. In this approach, we obtained a good agreement between data and theoretical results, for phase-shifts from elastic scattering and for ^{12}C 2^{+} inelastic excitation cross sections. Furthermore, this system presents resonances for the capture process, ^{12}C(α,γ)^{16}O, which were also well described by our theoretical calculations.

In the present work, we extend the model for the bare potential to heavier α-nucleus systems ($A \geqslant 58$). We take into account the couplings to the low-lying target states through CC calculations. To simulate the fusion process, we assume an internal shape for the imaginary part of the OP, with parameter values adjusted to obtain complete absorption of the flux that surpasses the ℓ-wave barriers, but without affecting the corresponding phase-shifts of the elastic S matrix. This behavior is consistent with the idea behind the barrier penetration model (BPM). In this context, our calculations do not involve any adjustable parameter and, therefore, we deal with theoretical predictions instead of data fits. We test the limits of the

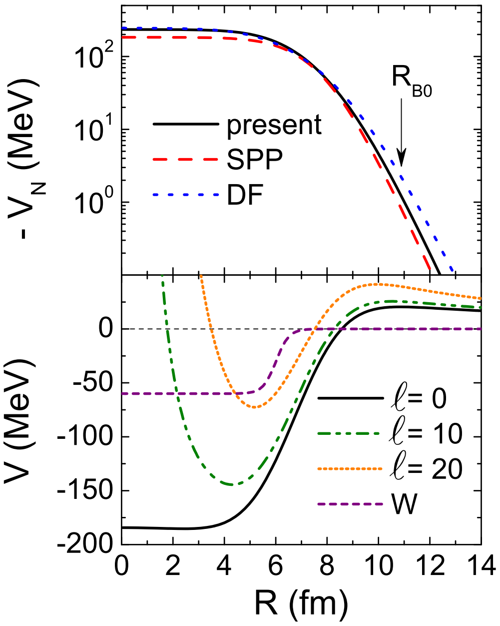

Figure 1. Top—modulus of the nuclear potential for the α + ^{208}Pb system according to the following models: present work, São Paulo potential (SPP) and Satchler and Love's double-folding (DF). The arrow indicates the approximate position of the *s*-wave barrier radius. Bottom—sum of the nuclear, Coulomb and centrifugal potentials for $\ell =$ 0, 10 and 20. Also the imaginary part of the OP is shown in the figure.

model in the description of elastic, inelastic as well as fusion cross section data for several systems.

2. The bare nuclear potential and the CC calculations

The nuclear potential assumed in the present work for the real part of the OP is given by [14, 17]

$$V_N(R) = \int \rho_1(r_1)\rho_2(r_2)v\left(\vec{R} - \vec{r}_1 + \vec{r}_2\right) \mathrm{d}\vec{r}_1\, \mathrm{d}\vec{r}_2, \tag{1}$$

with

$$v\left(\vec{r}\right) = -\, U_0 \mathrm{e}^{-(r/a)^2}, \tag{2}$$

where $U_0 = 87.226$ MeV, $a = 0.95$ fm, and the $\rho_i(r_i)$ represent the matter densities of the nuclei. As we have done in [14, 17], for the α particle we associate the matter density to the corresponding ^{4}He charge distribution (from [18]) multiplied by two (due to the normalization). We assume the systematics of the matter distributions of [6] for the heavy nuclei. We also calculate the Coulomb interaction through the DF method.

As an example, figure 1 (top) presents the nuclear potential for the α + ^{208}Pb system. Besides the present results (solid line), those from the SPP and Satchler and Love's DF potentials are shown. The DF was calculated assuming nucleon densities obtained with the Dirac–Hartree-BCS model [19]. At the region of the *s*-wave barrier radius (arrow in the figure), the three models provide similar shapes, with diffuseness values of about 0.64, 0.60

Table 1. Values of the excitation energies (MeV), deformation parameters (fm), $B(E2)$ (e^2b^2) and $B(E3)$ (e^2b^3) for the 2^+ and 3^- excited states of the heavy nuclei studied in this work. Also the values of the barrier radius (fm), height (MeV) and curvature (MeV) for the corresponding α-nucleus systems are presented in the table.

Nucleus	E_2^*	E_3^*	$B(E2)$	$B(E3)$	δ_2	δ_3	R_{B0}	V_{B0}	$\hbar w_0$
^{58}Ni	1.454	4.475	0.0695	0.0176	0.84	0.86	8.57	8.73	4.01
^{64}Zn	0.992	2.999	0.16	0.034	1.15	1.05	8.72	9.35	4.05
^{70}Ge	1.039	2.561	0.176	0.064	1.10	1.32	8.86	9.68	4.10
^{90}Zr	2.186	2.748	0.061	0.098	0.48	1.09	9.23	11.63	4.40
^{92}Mo	1.510	2.850	0.097	0.07	0.57	0.86	9.25	12.19	4.47
^{106}Cd	0.633	2.379	0.41	0.16	0.98	1.04	9.48	13.62	4.64
^{110}Cd	0.658	2.079	0.45	0.115	1.02	0.87	9.56	13.50	4.64
^{116}Cd	0.513	1.922	0.56	0.1	1.12	0.79	9.69	13.34	4.58
^{112}Sn	1.257	2.355	0.24	0.087	0.71	0.80	9.58	14.05	4.69
^{118}Sn	1.230	2.325	0.209	0.115	0.65	0.80	9.71	13.87	4.63
^{124}Sn	1.132	2.602	0.166	0.073	0.57	0.63	9.83	13.71	4.59
^{120}Te	0.560	2.083	0.77	0.06	1.19	0.53	9.72	14.41	4.71
^{130}Te	0.839	2.527	0.295	0.06	0.73	0.53	9.92	14.14	4.63
^{132}Ba	0.465	2.069	0.86	0.18	1.14	0.83	9.90	15.25	4.80
^{138}Ba	1.436	2.881	0.23	0.133	0.58	0.70	10.01	15.09	4.77
^{140}Ce	1.596	2.464	0.298	0.202	0.64	0.82	10.02	15.61	4.84
^{144}Sm	1.660	1.810	0.262	0.31	0.55	0.93	10.05	16.65	4.95
^{184}W	0.111	1.221	3.78	0.082	1.62	0.34	10.58	18.93	5.14
^{208}Pb	4.086	2.614	0.3	0.611	0.40	0.78	10.86	20.47	5.24
^{209}Bi	—	—	—	—	—	—	10.86	20.71	5.29
^{238}U	0.045	0.732	12.09	0.58	2.14	0.62	11.17	22.35	5.41

and 0.74 fm, but with strength values that differ by a factor of about 2.6 (between DF and SPP).

The CC calculations were performed in the context of the rotational model, using the FRESCO code [20], mostly considering the first 2^+ (quadrupole) and 3^- (octupole) target excited states. In some cases, we also included other states of the quadrupole band in the CC calculations. A few nuclei, among those that we have studied, are not well represented by the rotational model. Even so, as we will see, the effects of the inelastic couplings on the elastic and fusion channels are small in most cases. Thus, we consider that the assumption of the rotational model provides a reasonable estimate of the effects of the couplings even for nuclei that can not be considered as rotors.

The nuclear deformations, $\delta_2 = \beta_2 R_0$ and $\delta_3 = \beta_3 R_0$, were calculated from the corresponding Coulomb transition probabilities, $B(E2)$ and $B(E3)$, obtained from [21, 22], considering the correction due to the finite value of the diffuseness of the densities [23]. Table 1 provides the excitation energies of the 2^+ and 3^- states for the heavy nuclei studied in this work, and the corresponding values adopted for $B(E2)$, $B(E3)$, δ_2 and δ_3. Also the values of the s-wave barrier radius R_{B0}, height V_{B0} and curvature $\hbar w_0$ of the α-nucleus systems are presented in table 1.

3. The imaginary part of the OP and the BPM

As already commented, in most of the practical applications the imaginary part of the OP is treated phenomenologically. However, it has a significant effect on the cross sections obtained from optical model (OM) calculations. Thus, in data analyzes, realistic models should be assumed for the imaginary potential, otherwise important characteristics of the underlying fundamental physics might be hidden under the OM results. Indeed, this effect is not always taken into account. In this section, we discuss the criteria that we have adopted to determine the imaginary potential.

Assuming that all direct reaction channels with relevant cross sections are included explicitly in the coupled equations, the absorption of flux by the imaginary part of the OP should only correspond to the fusion process. Thus, we define the parameter values of the imaginary potential with the aim of reproducing the constraints involved in the hypotheses behind the BPM, as described below.

The BPM has been extensively used in fusion data analyzes (e.g. [24, 25]). The cross section is obtained from the barrier transmission coefficients through:

$$\sigma_{\mathrm{BPM}} = \frac{\pi}{k^2}\sum(2\ell + 1)T_\ell. \tag{3}$$

In the present work, the transmission probabilities are calculated from

$$T_\ell = \frac{1}{1 + \exp\left(C_\ell\right)}. \tag{4}$$

For ℓ-waves whose corresponding height is below the center of mass energy, the C_ℓ coefficients are calculated from the Hill–Wheeler formula for a parabolic barrier [26]

$$C_\ell = \frac{2\pi\left(E - V_{B\ell}\right)}{\hbar w_\ell}, \tag{5}$$

where $V_{B\ell}$ and $\hbar w_\ell$ are the height and curvature of the barrier, respectively. The curvature is related to the second derivative of the potential (nuclear + Coulomb + centrifugal) at the barrier radius $R_{B\ell}$ through

$$\hbar w_\ell = \sqrt{-\frac{\hbar^2}{\mu}\frac{\mathrm{d}^2 V}{\mathrm{d}R^2}}. \tag{6}$$

In the other case, $E < V_{B\ell}$, C_ℓ is calculated from the WKB approximation:

$$C_\ell = \int_{R_{\mathrm{in}}}^{R_{\mathrm{out}}} \sqrt{\frac{8\mu}{\hbar^2}[V(R) - E]}\ \mathrm{d}R, \tag{7}$$

where R_{in} and R_{out} are the inner and outer classical turning points, respectively.

Expressions (3)–(7) involve only the real part of the OP. On the other hand, within the OM, without couplings, the reaction cross section corresponds to the absorption arising from the imaginary part of the potential, and it is given by:

$$\sigma_R = \frac{\pi}{k^2}\sum(2\ell + 1)\left(1 - \left|S_\ell\right|^2\right), \tag{8}$$

where

$$S_\ell = \left|S_\ell\right|\ \mathrm{e}^{\mathrm{i}2\delta_\ell} \tag{9}$$

is the elastic S matrix. The S matrix, and consequently the reaction cross section, depends on both the real and imaginary parts of the OP.

The first constraint that we impose on the imaginary part of the OP is that, when the couplings are turned off, $\sigma_R \approx \sigma_{\mathrm{BPM}}$. More precisely, we force the $|S_\ell|$ values obtained from the OM calculations to be consistent with the transmission probabilities T_ℓ of the BPM, for all (or the more important) ℓ values. Thus, the strength of the imaginary potential, $W(R)$, should be large enough at internal distances to absorb all the flux therein, but small at the surface region, since the barrier transmission should be mostly related to the real part of the interaction.

As a second constraint, we impose the phase-shifts, δ_ℓ of (9), to be mainly related to the refraction due to the real part of the OP, so that the phenomenological imaginary part does not affect them significantly. Indeed, from a semi-classical point of view, the phase-shifts are related to the deflection function (or scattering angle, see e.g. [27]) through

$$\Theta(\ell) = \Theta_C(\ell) + 2\frac{\mathrm{d}\delta_\ell}{\mathrm{d}\ell}, \tag{10}$$

where $\Theta_C(\ell)$ is the Coulomb deflection function. Classically, the deflection angle can be obtained from an integral involving only the real part of the potential:

$$\Theta(b) = \pi - 2\int_{R_{\mathrm{out}}}^{\infty} \frac{b/R^2}{\sqrt{1 - b^2/R^2 - V(R)/E}}\,\mathrm{d}R, \tag{11}$$

where b is the impact parameter. Consequently, even in a quantum mechanical calculation, if the effect of the couplings is negligible, it is quite reasonable to require that the phenomenological imaginary part of the OP, which should only simulate the absorption of flux by the fusion, does not significantly affect the phase-shifts.

A rough estimate of the effect of the imaginary potential on the phase-shift can be obtained by considering the solution of the one-dimensional Schrödinger equation corresponding to uniform potential $-(V_0 + \mathrm{i}W_0)$:

$$-\frac{\hbar^2}{2\mu}\frac{\mathrm{d}^2\psi}{\mathrm{d}x^2} - \left(V_0 + \mathrm{i}W_0\right)\psi = E\psi \Longrightarrow \psi(x) = \mathrm{e}^{\mathrm{i}kx}, \tag{12}$$

where

$$k = \sqrt{\frac{2\mu\left(E + V_0 + \mathrm{i}W_0\right)}{\hbar^2}}. \tag{13}$$

For small W_0 values, (13) can be Taylor expanded to second order:

$$k \approx \sqrt{\frac{2\mu\left(E + V_0\right)}{\hbar^2}}\left\{1 + \frac{1}{8}\left[\frac{W_0}{E + V_0}\right]^2 + \mathrm{i}\frac{W_0}{2\left(E + V_0\right)}\right\}, \tag{14}$$

which results in

$$\psi(x) = \mathrm{e}^{-\gamma x}\mathrm{e}^{\mathrm{i}k'x}, \tag{15}$$

$$\gamma = k_0\frac{W_0}{2\left(E + V_0\right)}, \tag{16}$$

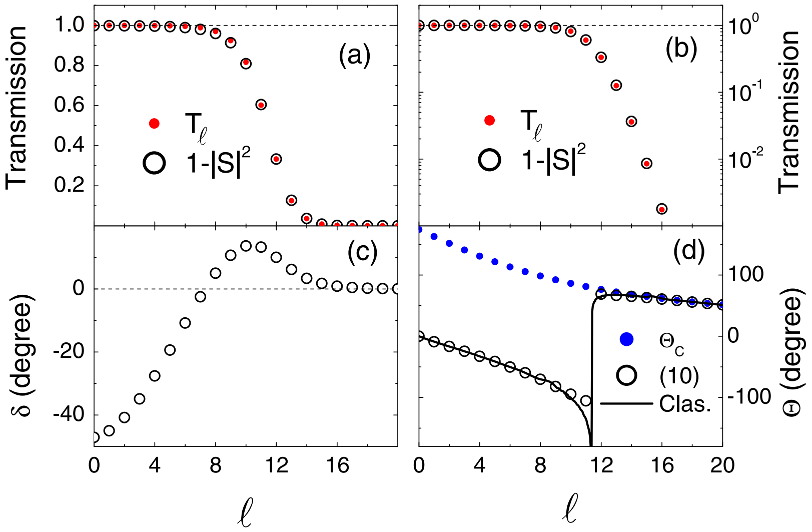

Figure 2. Transmission coefficients from BPM and OM calculations as a function of ℓ in (a) linear and (b) logarithmic scales, for α + ^{208}Pb at E_{Lab}= 27.6 MeV. (c) Nuclear phase-shifts from OM calculations. (d) Coulomb and total, from (10), deflection angles, as well as the classical results from (11).

$$k' = k_0\left\{1 + \frac{1}{8}\left[\frac{W_0}{E + V_0}\right]^2\right\}, \tag{17}$$

$$k_0 = \sqrt{\frac{2\mu\left(E + V_0\right)}{\hbar^2}}. \tag{18}$$

An inspection of (15) and (16) shows that the term of first order, $W_0/2(E + V_0)$, provides absorption of flux along the x-axis. On the other hand, the term of second order of (17), $\frac{1}{8}[W_0/(E + V_0)]^2$, affects the real part of the phase-shift. Thus, to fulfill the condition of keeping the phase-shifts invariable, we should impose $\frac{1}{8}[W_0/(E + V_0)]^2 \ll 1$. In practice, if $W_0 < (E + V_0)/3$ the modification is smaller than 1.4%.

We have assumed the Woods–Saxon shape for the imaginary part of the OP:

$$W(R) = -\frac{W_0}{1 + \exp\left[\left(R - R_{I0}\right)/a_I\right]}, \tag{19}$$

with $R_{I0} = r_{i0}(A_1^{1/3} + A_2^{1/3})$. With the aim of obtaining the conditions commented above, we performed many tests to define the corresponding best parameter values. They are: $W_0 = 60$ MeV, $r_{i0} = 0.8$ fm and $a_I = 0.25$ fm. We define this potential as the standard imaginary potential. As illustration, figure 1 (bottom) presents a comparison between $W(R)$ and the effective potentials (sum of the nuclear, Coulomb and centrifugal parts) for $\ell = 0$, 10 and 20, in the case of α + ^{208}Pb.

As an example of our tests, in figure 2 we present some results from BPM and OM (without couplings) calculations, obtained for the α + ^{208}Pb system at $E_{\mathrm{Lab}} = 27.6$ MeV. The OM calculations were performed with the standard imaginary potential. Figures 2(a) and (b),

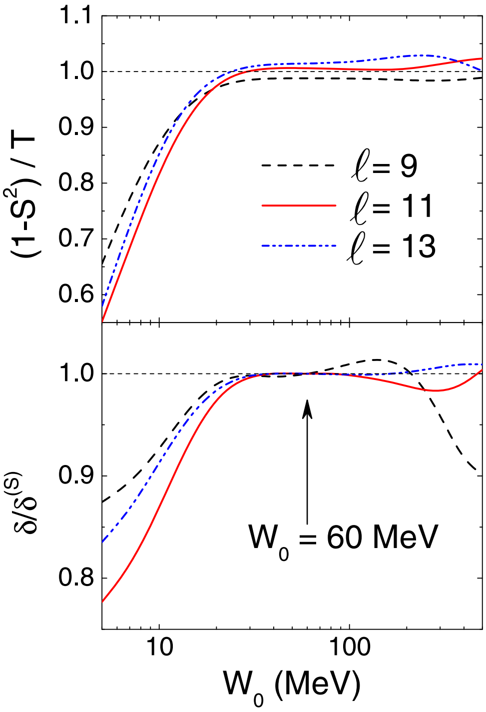

Figure 3. Values of $(1 - |S_\ell|^2)/T_\ell$ (top) and $\delta_\ell/\delta_\ell^{(S)}$ (bottom) as a function of W_0, for α + ^{208}Pb at E_{Lab}= 27.6 MeV. The results correspond to ℓ values around the grazing value. See text for details.

in linear and logarithmic scales, show that the T_ℓ results (from BPM) are very similar to the $1 - |S_\ell|^2$ ones (from OM). The grazing angular momentum, for which $T_\ell = 1/2$, is $\ell_g \approx 11$. Figures 2(c) and (d) present the nuclear phase-shifts and the deflection function, respectively. In (d), also the Coulomb and the classical deflection functions are shown. Clearly, the semi-classical deflection function, from (10), is similar to the classical one. This is an indication that the imaginary potential does not affect the phase-shifts.

Figures 3 and 4 illustrate the behavior of $(1 - |S_\ell|^2)/T_\ell$ and $\delta_\ell/\delta_\ell^{(S)}$ as a function of the values of the imaginary potential parameters, where $\delta_\ell^{(S)}$ is the phase-shift obtained with the standard values for the complete set of parameters. The results presented in these figures correspond to the case of α + ^{208}Pb, at E_{Lab} = 27.6 MeV, for ℓ values around the grazing. The calculations of S_ℓ and δ_ℓ were performed with standard values for two parameters (among W_0, r_{i0} and a_I) and varying the value of the remaining one. In figure 3 (top), we see that the absorption becomes approximately constant, and consistent with the BPM results, for $W_0 > 20$ MeV. On the other hand, for large values ($W_0 > 100$ MeV), the imaginary potential affects the phase-shifts significantly (see figure 3—bottom), and therefore this region is not compatible with our criteria for the OP. The arrow in this figure indicates the standard value adopted for W_0. Figure 4 was obtained with similar calculations as those of figure 3, but varying the r_{i0} and a_I parameters. Again the standard parameter values, indicated with arrows in the figure, are in regions which are in accordance with the criteria adopted for the imaginary part of the OP. In fact, these standard values were determined considering several similar tests performed for other energies and systems. The standard value adopted for the

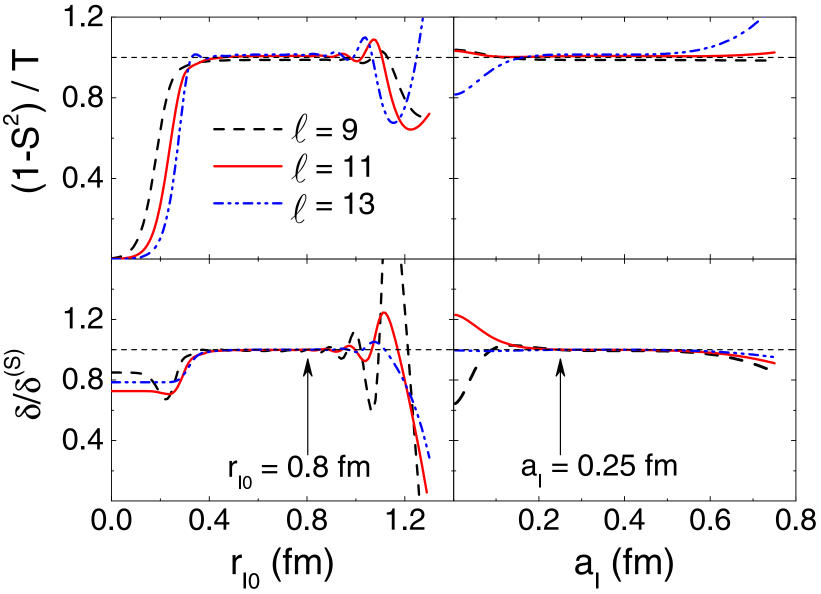

Figure 4. The same of figure 3, for the r_{i0} and a_I parameters.

diffuseness of the imaginary potential, $a_I = 0.25$ fm, is small compared with that obtained for the real part at the surface region (which is, for instance, 0.64 fm in the case of ^{208}Pb). A much larger value adopted for a_I would demand a smaller value for r_{i0}, and we have not found a set of values in this condition that works well for all systems analyzed here. The standard imaginary potential, obtained from tests considering only OM calculations without couplings, was then assumed in our CC calculations. Of course, within the CC calculations, due to the effect of the couplings, the reaction and the fusion cross sections are no longer equal, and they are not expected to be similar to the BPM one either.

4. Data analyzes

With the exception of the ^{209}Bi, we have chosen systems involving even–even nuclei as targets to perform our analyzes (see table 1). These nuclei have 0^+ ground-states, and low-lying 2^+ and 3^- excited states that we associate with the quadrupole and octupole bands. Besides these states, in a few cases we have also considered other states of the quadrupole band (4^+, 6^+, etc) in the CC calculations. We have selected elastic and inelastic scattering data, as well as experimental data related to the fusion process, for energies around the barrier, i.e. from sub-Coulomb to about 10 MeV above the *s*-wave barrier height. The total data set included in our analyzes is quite large, but we present here only a few figures with typical examples of the results obtained in our work.

Most of the elastic scattering data considered here have already been very well described in other works, through OM calculations with OP adjusted to fit the corresponding angular distributions. The idea employed in the present work is to analyze the data using a more fundamental approach. As earlier commented, our calculations do not involve any adjustable parameter to fit the data. Indeed, we perform CC calculations considering the more significant direct channel states, and assuming a model for the imaginary part of the OP with the particular characteristics discussed in the last section. The real part of the OP was successfully adopted in earlier analyzes for the $\alpha + \alpha$, ^{12}C systems, and here it is extended to heavier nuclei through the use of a realistic systematics of matter densities. Thus, we do not deal with data fits, but with comparison between theoretical predictions and experimental data. The goal of the work is thus to study the limits of the application of the theoretical model.

4.1. Fusion process

We associate the fusion cross section with the absorption of flux by the imaginary part of the OP. This theoretical cross section corresponds to the difference between the total reaction and the inelastic excitation cross sections. In the case of the α-nucleus fusion, the compound nucleus can decay through different modes: fission, evaporation of light particles, γ-rays. The main contribution among these modes depends on the bombarding energy, on the corresponding Q-values, as well as the total angular momentum distribution. Data are available for many of these decay modes for several α-nucleus systems. Hereafter, we discuss a few cases.

In figure 5, we present data of fission cross sections, for the case of $\alpha + {}^{238}$U [28–32], and of evaporation of one neutron, for $\alpha + {}^{132}$Ba [33]. The energy scale in this figure corresponds to the reduced energy that we define as:

$$E_{\text{red}} \equiv E_{c.m.} - V_{B0}. \tag{20}$$

We also show, in the figure, the fusion cross sections from the CC and OM (no couplings) calculations. Two types of CC calculations were performed: (i) considering only the 2^+ and 3^- states; and (ii) with a larger set of states (2^+, 3^-, 4^+ and 6^+). In the case of ^{238}U, the results of these two CC calculations are almost identical. At 8 MeV below the barrier, $E_{\text{red}} = -8$ MeV, the CC cross section is about 50% larger than the OM one, a difference almost indistinguishable in the scale of figure 5(a). At about 14 MeV above the barrier, the CC cross section is slightly smaller ($\approx$5%) than that of the OM, and this difference is responsible for a better agreement between the CC and experimental results than in the case of the OM (see figure 5(c) at the region of high energies). The agreement between data and theoretical predictions is also good in the case of ^{132}Ba. Here, a quite small difference between the results of the two types of CC calculations can hardly be observed in figure 5(d).

The ^{238}U and ^{132}Ba nuclei have quite large nuclear deformations and small 2^+ excitation energies, and therefore the effect of the couplings for these nuclei should be more significant than in the cases of the other nuclei of table 1. Even so, as shown in figure 5, the effect of the couplings on the fusion cross sections for ^{238}U and ^{132}Ba are small. In fact, this effect is even smaller for the other systems. Thus, in the next figures we only show the results of the CC calculations, since they are almost indistinguishable from the OM ones.

Data for ^{209}Bi [34–39] and ^{208}Pb [34, 40, 41] are presented in figure 6 top and bottom, respectively. In the case of ^{209}Bi, the main contribution to the fusion process corresponds to the evaporation of neutrons (the respective thresholds are indicated by arrows in the figure). The CC results for fusion account for the data in the entire energy range. For ^{208}Pb, the theoretical calculations agree with the one neutron evaporation cross sections at the sub-barrier energy region. However, at the region $E_{\text{red}} \approx 3.5$ MeV, the sum of the one and two neutrons experimental cross sections (star symbols in the figure) is significantly smaller than the theoretical fusion cross section. On the other hand, these theoretical values are in agreement with the reaction cross section data of [41] (open circles in the figure). Note that the calculated inelastic cross sections (dashed orange line in the figure) are very small in this energy region and, therefore, the fusion and reaction cross sections should be practically identical, as in fact they are. Thus, the sum of the one and two neutrons cross section data

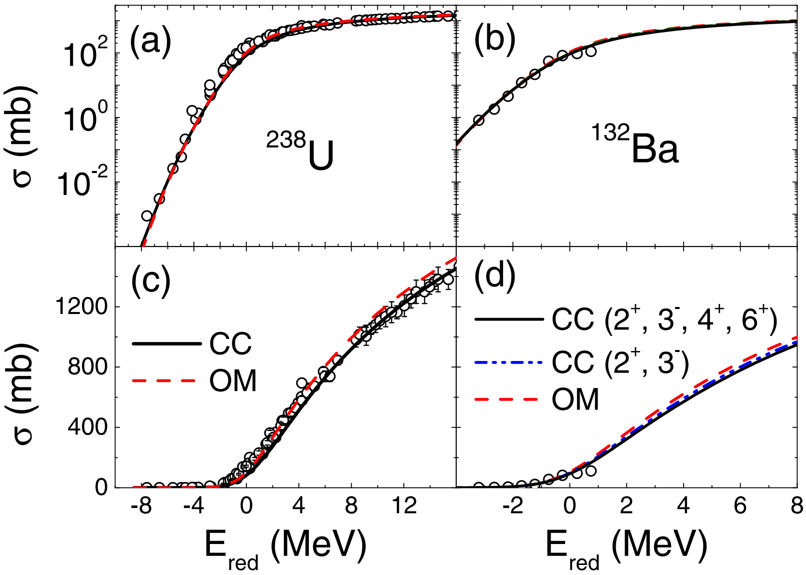

Figure 5. Cross section data for fission in α + ^{238}U [28–32] and one neutron evaporation in α + ^{132}Ba [33], as a function of the reduced energy. Note the change from logarithmic (top) to linear (bottom) scales. The lines correspond to the theoretical predictions for the fusion cross section, from CC and OM (no couplings) calculations.

from [34, 40] seems to be inconsistent with the reaction data of [41]. Perhaps, another evaporation mode has significant contribution to the fusion cross section in this energy region.

Figure 7 exhibits cross section data for some modes of decay of the compound nucleus in the cases of α impinging on ^{144}Sm [42, 43], ^{106}Cd [44] and ^{112}Sn [45–47]. For these three systems, at low energies the largest contribution to the fusion arises from the capture process, i.e. from the decay through the emission of gamma rays. For energies above the corresponding threshold (arrows in the figure), the one neutron evaporation becomes the dominant process (see figures 7(a) and (b)). In the case of ^{112}Sn, there are data for the capture process at low [45, 46] and high [47] energies, represented in figure 7(c) by closed and semi-closed stars, respectively. Clearly, these data sets present discrepancies of about one order of magnitude. Large differences of normalization relative to the data of [47] were already reported in [48]. In figure 7(d), we have re-normalized the data of [47] by a factor of 10. With this, an inspection of figures 7(a), (b) and (d) shows that the theoretical fusion cross sections are in good agreement with the data for the three systems.

The theoretical fusion cross sections agree with the data of the capture process [49], in the case of ^{70}Ge at sub-barrier energies (see figure 8(a)). For this system, there are data sets for one neutron evaporation at high energies from [50] and [51], represented by closed and semi-closed circles in figure 8(a), that significantly differ from each other. This fact makes it difficult to ascertain the quality of the theoretical predictions at these energies. The case of ^{64}Zn, for which there are data for the fusion process [52, 53] besides those for evaporation [54–57], is shown in figure 8(b). The theoretical fusion cross sections agree well with the one proton channel at sub-barrier energies, except for very low energies where the capture process probably plays an important role. Also for this case of ^{64}Zn, different data sets at higher energies present some discrepancies. As shown in figure 8(c), and in the magnification of the

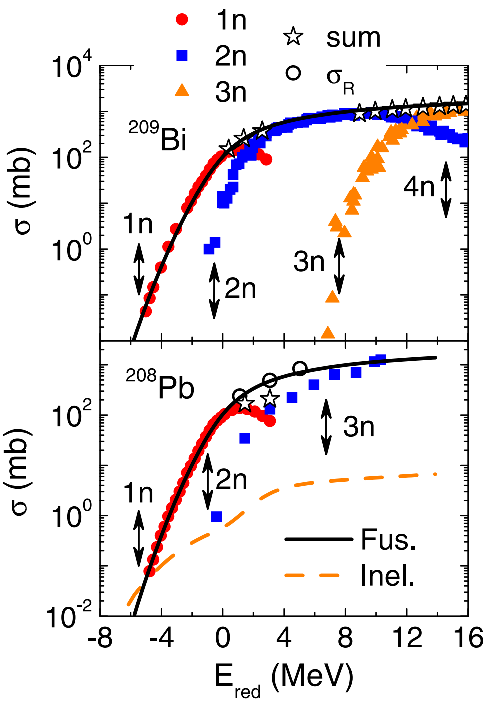

Figure 6. Cross section data for neutrons evaporation in (top) α + ^{209}Bi [34–39] and (bottom) α + ^{208}Pb [34, 40]. The star symbols in the figure represent the sum of these different contributions to the fusion cross sections. The lines correspond to the CC results for fusion and inelastic (2^++ 3^-) cross sections. In the case of ^{208}Pb, we also present data for the reaction cross section [41]. The arrows in the figure indicate the approximate positions of the energetic thresholds for the respective neutrons channels.

figure 8(d), the theoretical predictions are in good agreement with the data of [55, 58–61] in the case of ^{58}Ni.

4.2. Inelastic scattering process

Figure 9 presents data [62–64] and theoretical cross sections for the inelastic excitation of the 3^- state of ^{208}Pb at several reduced energies. Considering the lack of adjustable parameters, the agreement between data and predictions is quite good, for below-barrier as well as for above-barrier energies.

In figure 10, we show data for the inelastic excitation of ^{184}W [65] and ^{138}Ba [66]. In the case of ^{184}W, besides the 2^+ and 3^- states, there are also data for the 4^+ quadrupole band state. The corresponding theoretical calculations result in a reasonable description of the data sets for both nuclei.

Data [65, 67] and theoretical predictions for the inelastic excitation of the first 2^+ state of ^{64}Zn and ^{58}Ni are presented in figure 11. There is a good agreement between the theoretical and experimental results at the region of forward angles, but the data present much larger cross sections in comparison with the theoretical values at backward angles. Similar behavior is also found in the case of the elastic scattering process, as discussed in the next subsection.

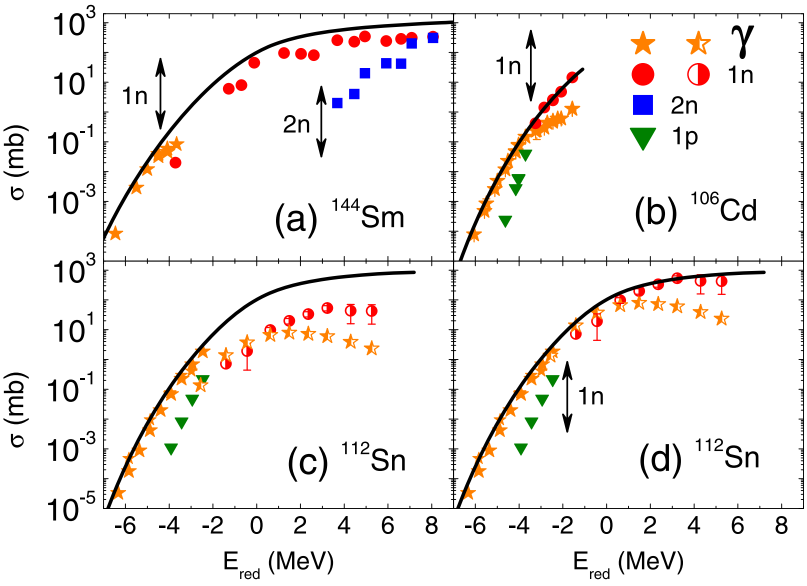

Figure 7. Cross section data for some modes of decay of the compound nucleus for α on (a) ^{144}Sm [42, 43], (b) ^{106}Cd [44], (c) and (d) ^{112}Sn. The lines correspond to the theoretical fusion cross sections and the arrows represent the thresholds of some modes. In (c), the closed symbols correspond to the data of [45, 46], while the semi-closed ones are from [47]. In (d) the data of [47] are re-normalized by a factor of ten.

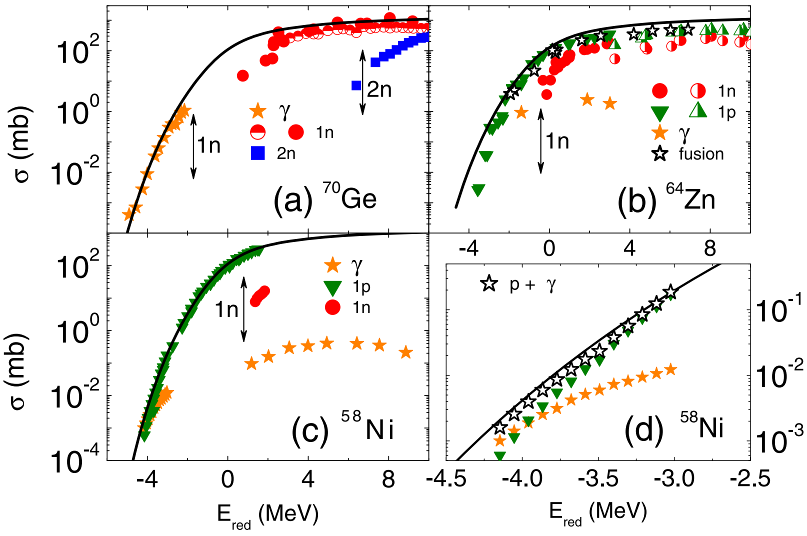

Figure 8. Cross section data for some modes of decay of the compound nucleus for α on (a) ^{70}Ge [49–51], (b) ^{64}Zn [52–57], (c) and (d) ^{58}Ni [55, 58–61]. The lines correspond to the theoretical fusion cross sections and the arrows represent the thresholds of the neutron and multiple neutron evaporation energies.

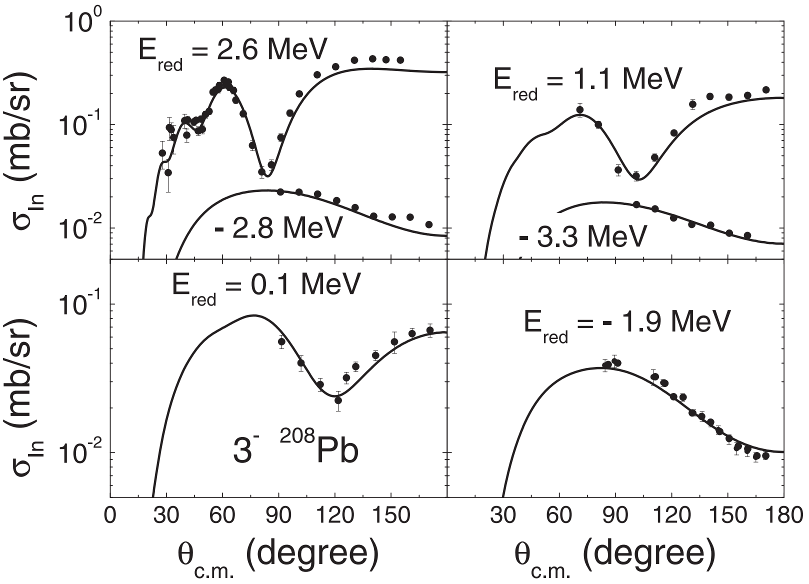

Figure 9. Experimental angular distributions [62–64] and corresponding theoretical predictions for the inelastic excitation of the 3^- ^{208}Pb state at several reduced energies.

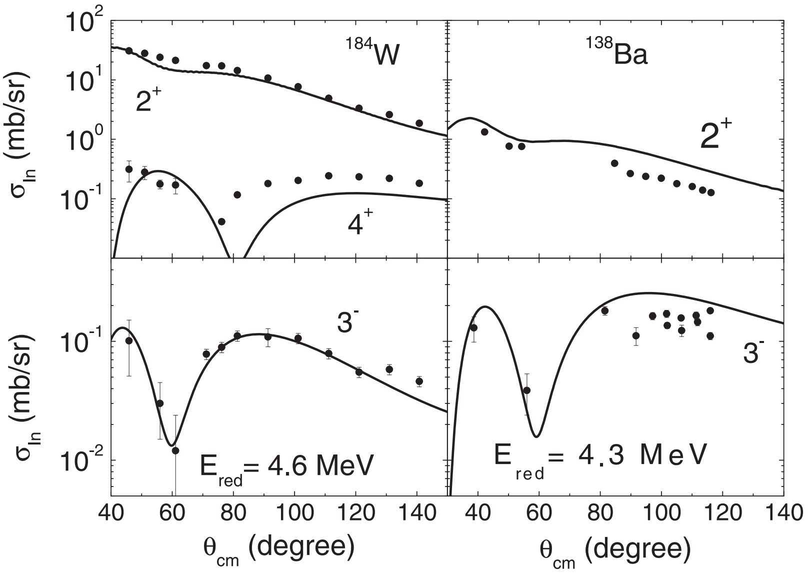

Figure 10. The same as figure 9, but instead for the 2^+, 3^- and 4^+ states of ^{184}W [65], and for the 2^+ and 3^- states of ^{138}Ba [66].

In figure 12, we present new data for the 2^+ inelastic excitation of ^{120,130}Te at $E_{\text{Lab}} = 17$ and 27 MeV. These data were obtained from re-analyzes of the spectra of the experiments reported in [68]. The overall agreement between data and theory (solid lines in figure 12) is good, except at the backward angular region for the higher energy: $E_{\text{Lab}} = 27$ MeV.

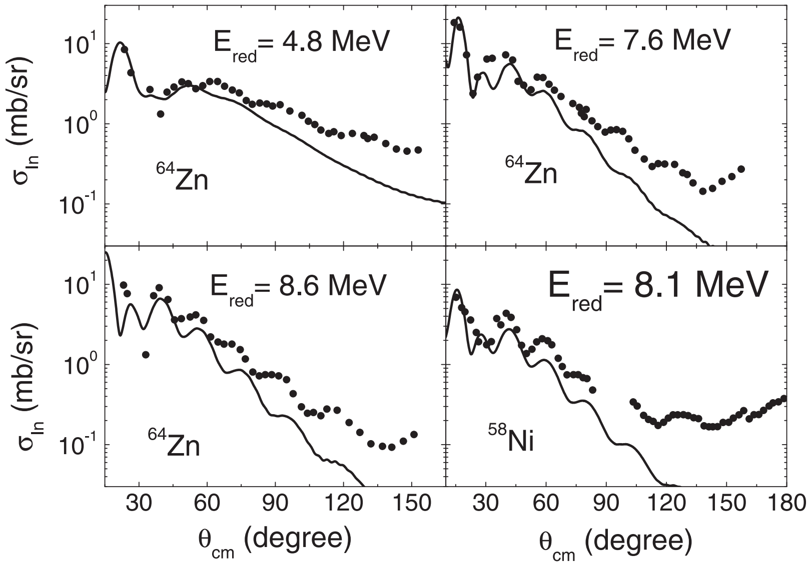

Figure 11. Experimental angular distributions [65, 67] and corresponding theoretical predictions for the inelastic excitation of the 2^+ state of ^{64}Zn and ^{58}Ni at several reduced energies.

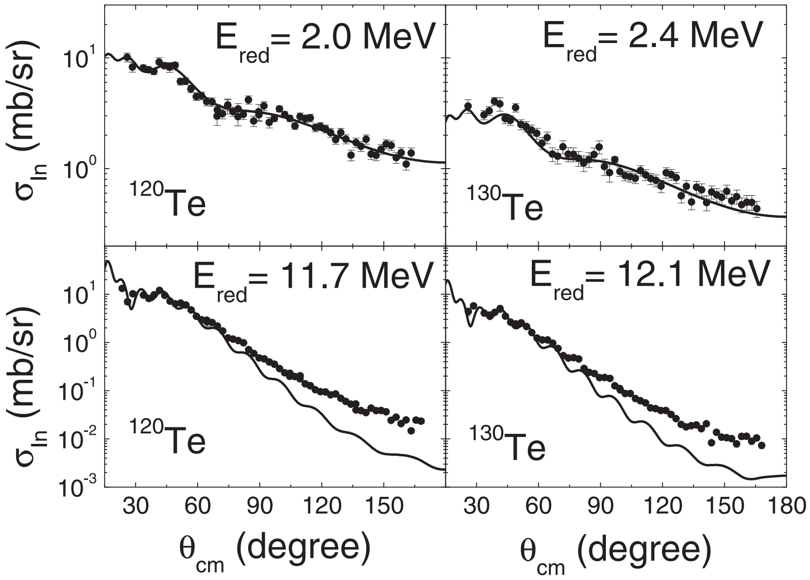

Figure 12. Experimental angular distributions and corresponding theoretical predictions for the ^{120,130}Te 2^+ inelastic excitations at $E_{\mathrm{Lab}} = 17$ and 27 MeV. The corresponding reduced energies are indicated in the figure.

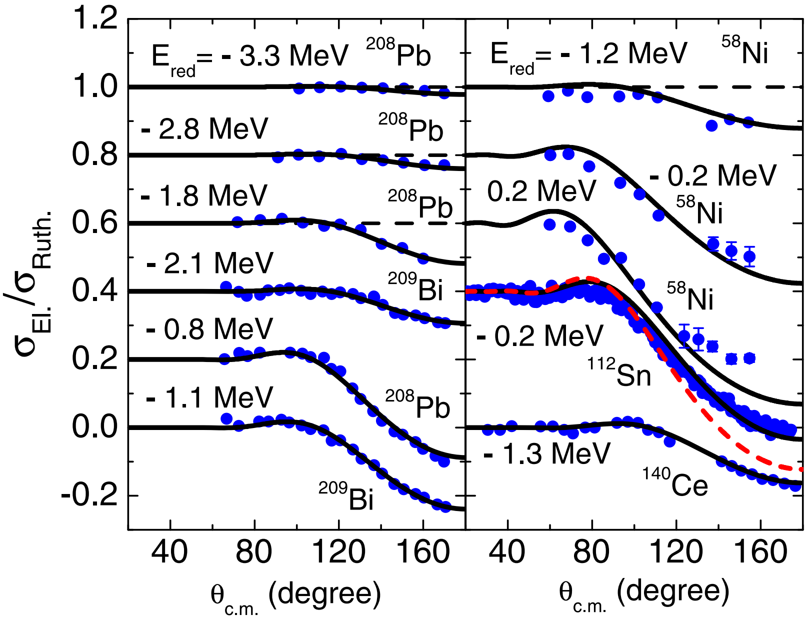

Figure 13. Experimental [11, 34, 64, 69, 70] and CC theoretical angular distributions, at the region of low reduced energies, for the elastic scattering of α on the target nuclei indicated in the figure. In the case of ^{112}Sn, we also show the theoretical results obtained from OM calculations (dashed red line). For several angular distributions, the cross sections are displaced by a constant value.

4.3. Elastic scattering process

Figure 13 presents elastic scattering data [11, 34, 64, 69, 70] and corresponding theoretical predictions for several systems, at the region of low reduced energies (from below up to the barrier height). In order to not overwrite the results, for several angular distributions the cross sections are shifted by a constant value. Except in the case of ^{112}Sn at $E_{\rm red} = -0.2$ MeV, the theoretical OM results without couplings are almost indistinguishable from the CC ones. As can be observed in the figure, at this low energy region the CC results are in quite good agreement with the data, except by small discrepancies at backward angles for ^{58}Ni at $E_{\rm red} = 0.2$ MeV, which corresponds to the distribution measured at the highest reduced energy shown in the figure.

Figure 14 presents excitation functions of elastic scattering at backward angles for several systems: ^{90}Zr and ^{92}Mo at $\theta_{c.m.} \approx 170^{\rm o}$ [71], ^{110}Cd at $\theta_{c.m.} \approx 175^{\rm o}$ [72], ^{116}Cd, ^{112}Sn, ^{124}Sn, ^{130}Te and ^{208}Pb at $\theta_{c.m.} \approx 179^{\rm o}$ [73]. Apart from the case of the ^{90}Zr, the data sets are well described by the theoretical cross sections. The CC predictions slightly underestimate the cross sections at the higher energies, a region where the cross sections are small compared to Rutherford scattering.

In figure 15(a), we show data [74] and theoretical CC results for the excitation functions at $\theta_{c.m.} \approx 72^{\rm o}$, $92^{\rm o}$, $122^{\rm o}$ and $165^{\rm o}$ in the case of α + ^{124}Sn. Again the agreement between the data and theoretical cross sections is reasonable, and the CC results are slightly smaller than the data for the backward angles at the higher energies. Indeed, there is a correlation between the absolute value of the cross section and the discrepancy between theoretical and experimental results. We illustrate this behavior in figure 15(b), where the ratio between

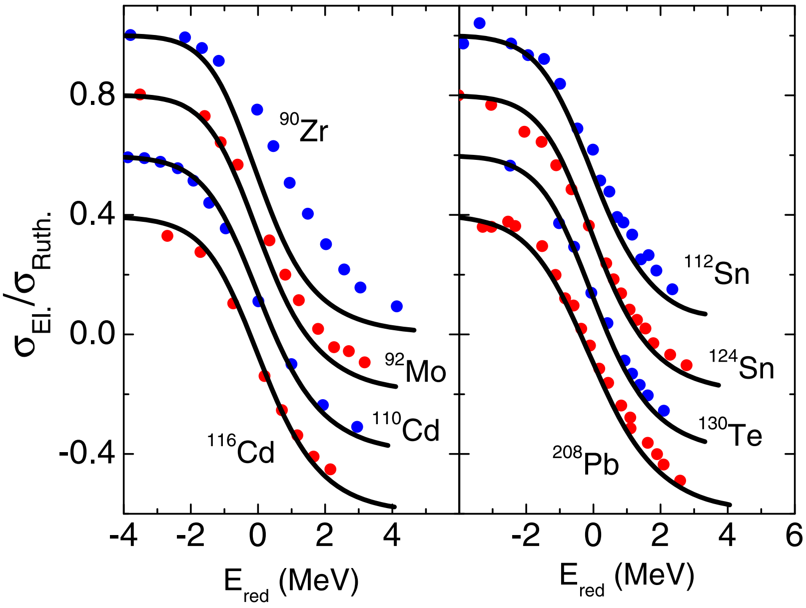

Figure 14. Experimental [71–73] and theoretical excitation functions for the elastic scattering of several systems at backward angles. In several cases, the cross sections are displaced by a constant value.

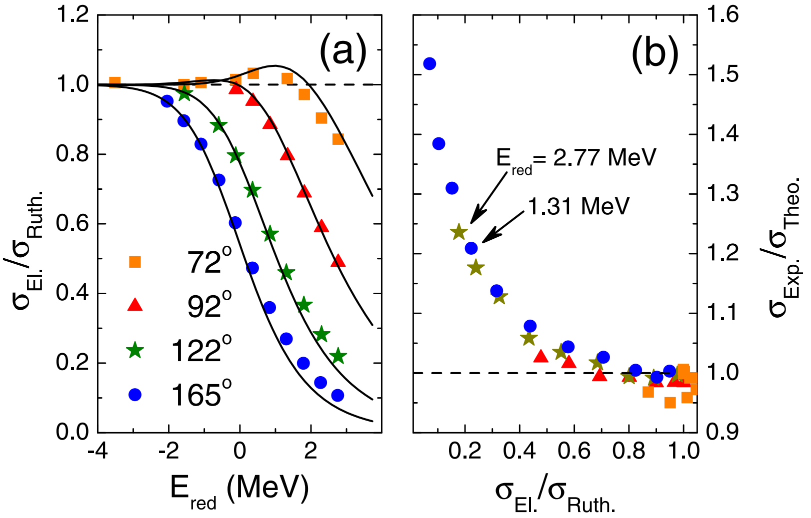

Figure 15. (a) Experimental [74] and theoretical excitation functions at several angles for the α + ^{124}Sn system. (b) The ratio between the experimental and theoretical cross section values as a function of the CC cross section.

experimental and theoretical cross sections $\sigma_{\text{Exp.}}/\sigma_{\text{Theo.}}$ is presented as a function of the theoretical $\sigma_{\text{El.}}/\sigma_{\text{Ruth.}}$ values. One can see a smooth behavior of this ratio, which seems to be independent of the angle and energy. For example, the arrows in the figure indicate points that correspond to different energies and angles, which have approximately the same ratio values

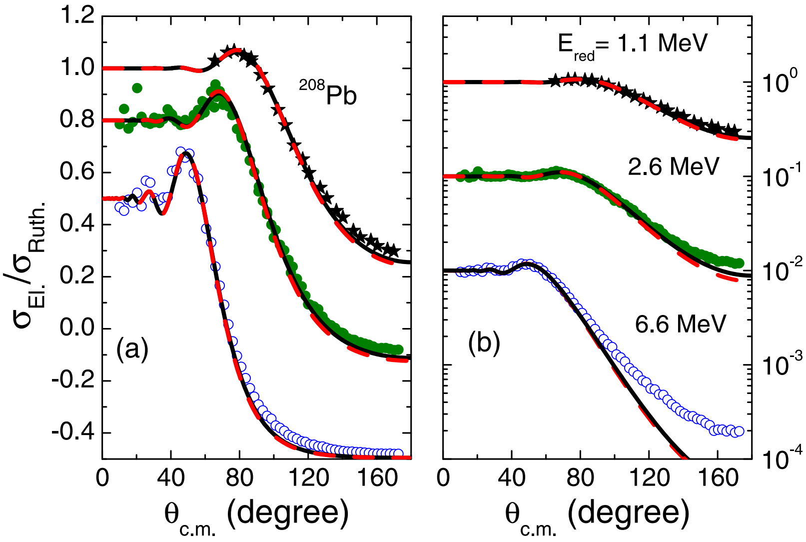

Figure 16. Experimental angular distributions [34, 63, 75] for the α + ^{208}Pb system at three reduced energies. The solid black and dashed red lines represent the results of the CC and OM calculations, respectively. Note the change from (a) linear to (b) logarithmic scale. To avoid superposition, the cross sections for E_{red}= 2.6 and 6.6 MeV are (a) displaced by 0.2 and 0.5, and (b) multiplied by 10^{-1} and 10^{-2}, respectively.

(and similar theoretical and experimental cross sections). This is an indication that our theoretical predictions fail when dealing with quite small elastic scattering cross sections.

Experimental angular distributions [34, 63, 75] for α + ^{208}Pb at energies above the barrier are presented in figure 16, in (a) linear and (b) logarithmic scales. To avoid superposition, the cross sections for E_{red}= 2.6 and 6.6 MeV are (a) displaced and (b) multiplied by constant factors. The solid black and dashed red lines in the figure represent the CC and OM results, respectively. The theoretical predictions agree with the data over the region where the elastic cross section has the same order of magnitude as Rutherford scattering. On the other hand, the CC predictions underestimate the data where the cross section is small, with larger discrepancies for smaller cross sections. Other examples for several systems and energies with similar behavior are presented in linear and logarithmic scales in figures 17 and 18, respectively (data from [11, 65–68, 70, 76, 77]).

5. Discussion

As reported in the last section, the overall agreement between theoretical predictions and data related to the fusion process is quite good for all systems studied in this work. Similar results have also been obtained for the 2^+ and 3^- inelastic target excitations, except for some discrepancies observed at high energies and backward angles. In the case of elastic scattering, the data are well described by the theory where the experimental cross section has the same order of magnitude of the Rutherford one, but the CC predictions are significantly smaller than the data over the region of very small cross sections. Certainly, the failure in describing inelastic cross sections at high energies and backward angles is related to the similar results concerning the elastic scattering, since there is a strong correlation between these two processes. In this section, we investigate the reasons for this failure. There are three fundamental

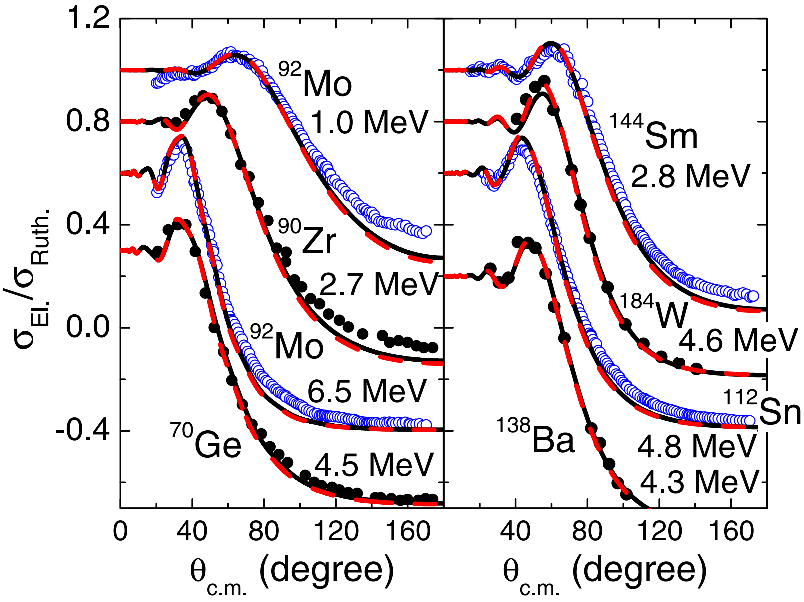

Figure 17. Experimental angular distributions for the elastic scattering of α on ^{92}Mo (two different reduced energies) [76], ^{90}Zr [70], ^{70}Ge [70], ^{144}Sm [11], ^{184}W [65], ^{112}Sn [77] and ^{138}Ba [66]. The solid black and dashed red lines represent the results of the CC and OM calculations, respectively. To avoid superposition, the cross sections are displaced by constant factors.

components in the theoretical model: (1) the nuclear interaction, (2) the absorption related to the imaginary part of the OP, and (3) the couplings. Something is wrong or missing in one (or more) of these components. In what follows, we discuss each of them separately.

5.1. The nuclear interaction

First, we focus on the real part of the interaction. We choose, as illustration of our analyzes, the case of the α + ^{208}Pb system, for which fusion, inelastic and elastic scattering data are shown in figures 6, 9, 13 and 16. As is often done in data analyzes, we have adjusted the shape and normalization of the nuclear potential in order to fit the elastic scattering data set of $E_{\mathrm{Lab}} = 27.6$ MeV ($E_{\mathrm{red}} = 6.6$ MeV). In our calculations, the shape was varied by considering the diffuseness of the ^{208}Pb matter distribution as a free parameter. We obtained a diffuseness value of 0.35 fm (for the ^{208}Pb matter density) with a normalization factor of 3.7 for the potential. This diffuseness value is much smaller than the realistic average value adopted in the systematics of densities of [6]: 0.56 fm. The corresponding diffuseness of the nuclear potential at the barrier radius is about 0.45 fm, again a small value in comparison with those from the realistic potentials shown in figure 1 (from 0.60 to 0.74 fm). In figure 19, we present three elastic scattering angular distributions for the α + ^{208}Pb system. The black lines in this figure correspond to the CC cross sections obtained with the standard nuclear potential, while the red ones arise from the calculations with the adjusted potential. Parts (a) and (c) of the figure correspond to the adjusted distribution of $E_{\mathrm{red}} = 6.6$ MeV, in linear and logarithmic scales, respectively. The adjusted potential provides a good description of the data for this energy, with some discrepancy at the region of the Coulomb rainbow (see figure 19(a) at $\theta \approx 50^{\circ}$), which, on the other hand, is well described by the standard calculations. However,

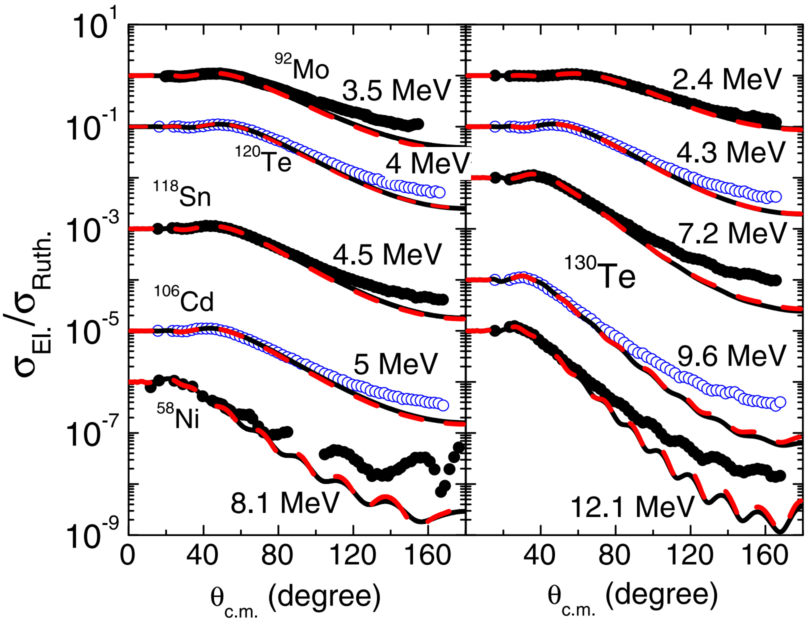

Figure 18. Experimental angular distributions for the elastic scattering at different reduced energies of α on ^{58}Ni [67], ^{92}Mo [76], ^{106}Cd [68], ^{118}Sn [68], ^{120}Te [68] and ^{130}Te (five energies) [68]. The solid black and dashed red lines represent the results of the CC and OM calculations, respectively. To avoid superposition, the cross sections are multiplied by factors of ten.

the predictions resulting from the adjusted potential clearly fail when extrapolated to other energies, as illustrated in figures 19(b) and (d). Furthermore, as shown in figure 20, the predictions for the fusion cross sections at sub-barrier energies obtained with the adjusted potential are significantly worse than those from the standard potential. Thus, we conclude that a modification only in the real part of the OP can not improve the description of the complete data set.

5.2. The absorption

Now we focus on the absorption provided by the imaginary part of the OP. We still analyze, as an example, the case of α + ^{208}Pb at $E_{\mathrm{red}} = 6.6$ MeV. At this energy, the total inelastic cross section is very small (see figure 6 bottom) and, therefore, the reaction and fusion cross sections have practically the same values. As illustrated in figure 16(b) for $E_{\mathrm{red}} = 6.6$ MeV, the experimental elastic scattering cross sections are much larger than the CC ones at the region of backward angles. This means that the theoretical model slightly overestimate the absorption of flux from the elastic channel to the fusion. We evaluated the integral of the difference between the data and the CC elastic scattering cross sections at this backward angular region ($65^{\circ} \leqslant \theta \leqslant 180^{\circ}$). We obtained a value of about 50 mb. One could raise the hypothesis that this 'extra' cross section is related to the fusion-elastic process (elastic channel as result of the decay). In order to check this possibility, we estimated the corresponding contribution to the elastic scattering cross section using the Empire code [78, 79]. We obtained 1.43 mb (1.395 mb from pre-equilibrium and 0.035 mb from the compound-elastic),

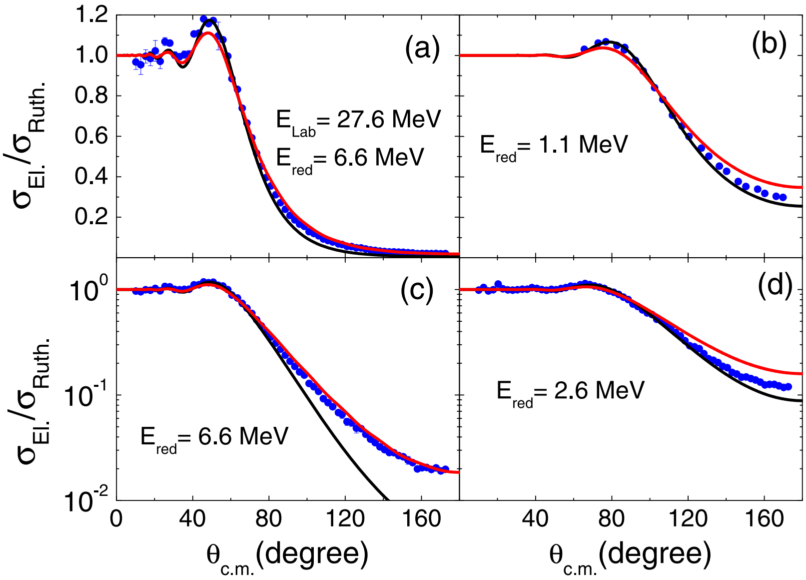

Figure 19. Elastic scattering angular distributions for the α + ^{208}Pb system at three different energies. Note the change from linear (top) to logarithmic (bottom) scales. The black lines correspond to the CC predictions obtained with the standard nuclear potential, while the red ones are related to the results obtained with the potential adjusted to fit the data of $E_{\rm Lab}$= 27.6 MeV.

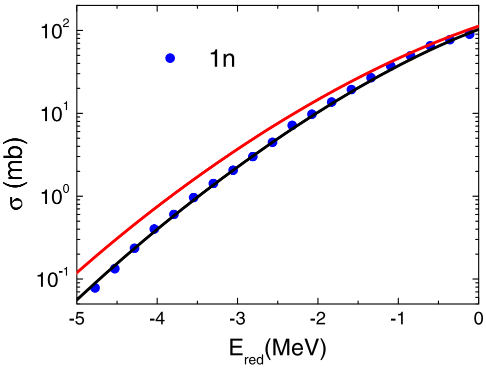

Figure 20. Cross section data for evaporation of one neutron in α + ^{208}Pb. The black line corresponds to the CC fusion cross sections obtained with the standard nuclear potential, while the red one is related to the results obtained with the potential adjusted to fit the elastic scattering data set of $E_{\rm Lab}$= 27.6 MeV.

a value almost two orders of magnitude smaller than the above commented 50 mb and, therefore, that hypothesis is discarded.

The value of 50 mb evaluated for the integral of the difference between data and CC elastic scattering cross sections corresponds to approximately 5.6% of the theoretical fusion (or reaction) cross section. As the reaction cross section is related to the modulus of the S matrix through (8), we have an indication that the detected problem with the description of the

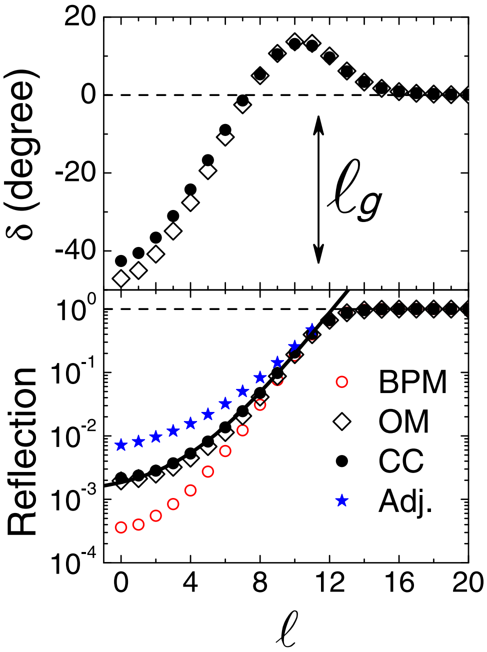

Figure 21. Phase-shifts (top) and reflection coefficients (bottom) as functions of ℓ for α + ^{208}Pb at $E_{\text{red}} = 6.6$ MeV. The figure contains the results from the BPM, OM and CC approaches, as well as the adjusted values obtained from the fit of the corresponding experimental elastic scattering angular distribution. The arrow indicates the approximate position of the grazing angular momentum. The solid line in the figure corresponds to the results of the function (21) with $P_1 = 0.0352$, $P_2 = 0.6072$ and $P_3 = 2.532$.

elastic scattering could be associated with the $|S_\ell|$ values, i.e. with the absorption. The parameters of $W(R)$ were adjusted to produce total absorption of the flux that surpasses the ℓ-wave barriers. Thus, we consider, as described below, the possibility that the absorption can be incomplete.

In figure 21, we show the phase-shifts (top) and the reflection coefficients (bottom) as functions of ℓ, for α + ^{208}Pb at $E_{\text{red}} = 6.6$ MeV. In the BPM approach, the reflection coefficient is obtained from $R_\ell = 1 - T_\ell$, while within the CC and OM formalisms we have $R_\ell = |S_\ell|^2$. According to the discussion above, we tried to fit the elastic scattering data set at $E_{\text{red}} = 6.6$ MeV, by increasing the $|S_\ell|$ values (and, therefore, increasing R_ℓ) relative to the CC results, in a region of ℓ which is discussed below. In these fits, the theoretical cross sections were calculated directly from the S matrix, assuming the phase-shifts obtained from the CC calculations, and with $|S_\ell|$ values which were allowed to vary with the purpose of adjusting the data.

In the calculations of elastic scattering cross sections, we can split the angular momenta into two regions: $\ell < \ell_g$ (for which $E_{c.m.} > V_{B\ell}$) and $\ell \geqslant \ell_g$ ($E_{c.m.} \leqslant V_{B\ell}$), where the grazing angular momentum is defined from $R_{\ell_g} = T_{\ell_g} = 1/2$. For α + ^{208}Pb at $E_{\text{red}} = 6.6$ MeV, ℓ_g is between 11 and 12. The experimental fusion and elastic scattering cross sections are very well described by the CC predictions at the sub-barrier energy region ($E_{c.m.} < V_{B0}$), which is an indication that the theoretical model provides good results for ℓ values with $E_{c.m.} \leqslant V_{B\ell}$, i.e. for $\ell \geqslant \ell_g$. Thus, in the data fits, we assumed the CC results for the $|S_\ell|$ in the region of $\ell \geqslant \ell_g$,

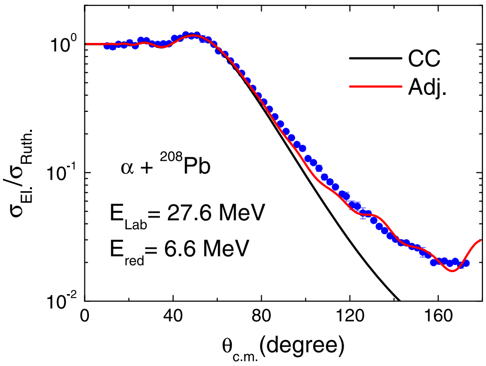

Figure 22. Elastic scattering angular distribution for $\alpha + {}^{208}\text{Pb}$ at $E_{\text{red}} = 6.6$ MeV. The black line represents the CC results while the red one corresponds to the cross sections obtained with the adjusted S matrix.

and we allowed variations of the $|S_\ell|$ values only for $\ell < \ell_g$, i.e. for $\ell \leqslant 11$ in the case of ^{208}Pb at $E_{\text{red}} = 6.6$ MeV.

In principle, all the twelve values of $|S_\ell|$ for $\ell \leqslant 11$ could be be considered as free parameters in the fit of the experimental angular distribution. Nevertheless, this procedure would certainly result in ambiguities in the determination of the best parameter values, and it also could provide unrealistic sharp structures in the behavior of $|S_\ell|$ as a function of ℓ. Thus, we have adopted another method to fit the data, with a smaller number of degrees of freedom, that provides a smooth behavior of the $|S_\ell|$ values. As illustrated through the solid line in figure 21 (bottom), the $|S_\ell|$ obtained from the CC calculations are described well (for $\ell \leqslant 11$) by the function (21) with the following parameter set: $P_1 = 0.0352$, $P_2 = 0.6072$ and $P_3 = 2.532$.

$$\left|S_\ell\right| = P_1 + P_2 \mathrm{e}^{(\ell-11)/P_3}. \tag{21}$$

Thus, we have assumed this function, with adjustable parameters P_1, P_2 and P_3, to fit the data and obtained a reasonable data fit with the following values: $P_1 = 0.071$, $P_2 = 0.6144$, $P_3 = 2.88$. The data fit is illustrated by the red line in figure 22. The figure also contains the CC results (black line). The corresponding adjusted R_ℓ values are presented as star symbols in figure 21 (bottom).

The reaction cross section obtained with the adjusted S matrix is 4.3% smaller than that arising from the CC calculations. Small differences like this are difficult to detect through the comparison between theoretical and experimental results for fusion cross sections. On the other hand, if reliable theoretical predictions for cross sections are available, the corresponding effect on the elastic scattering at backward angles can be clearly observed.

Thus, we consider that the detected failure in describing the elastic scattering data with our CC calculations could be associated with the incomplete absorption of flux (that surpasses the barrier) from the elastic channel to the fusion. The reason for this slight nuclear transparency in frontal collisions ($\ell < \ell_g$) may be related to the polarization arising from the couplings between the fusion and the elastic scattering channels. Indeed, through the dispersion relation, it is expected a short-range real potential connected with the short-range fusion absorption. Besides the absorption, the compound-nucleus formation should involve virtual excitation processes, from which a repulsive short-range contribution to the real potential should emerge. This might slightly modify the ion–ion potential at small

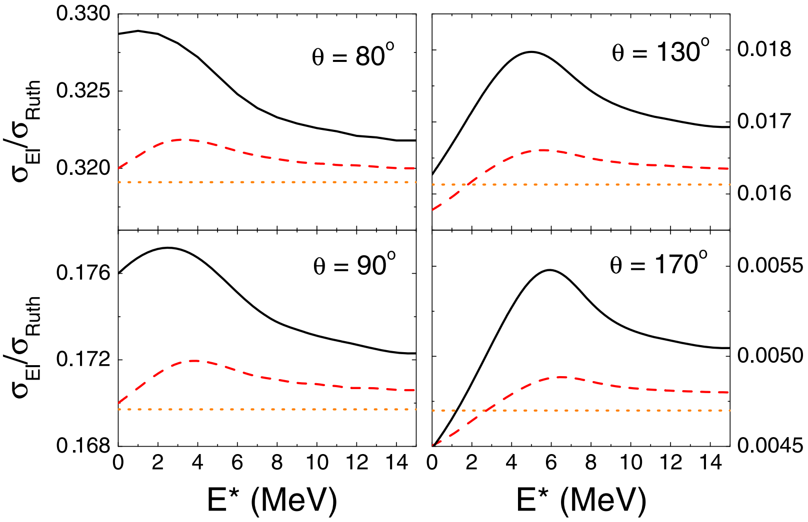

Figure 23. Elastic scattering cross sections for the α + ^{208}Pb system at $E_{\mathrm{Lab}} = 27.6$ MeV, for four different scattering angles, as a function of the excitation energy of the inelastic state. The solid and dashed lines represent the results obtained with the coupling to the 3^- and 2^+ states, respectively. For comparison, the dotted lines represent the cross sections obtained without couplings.

internuclear distances, affecting the trajectories of low partial waves. This effect is often neglected since the absorption is only used to simulate an irreversible nature of the fusion process at short-range distances, as we have also assumed in the present work. On the other hand, the nuclear transparency may also be related to the couplings between the elastic and low-lying inelastic channels, as discussed below.

5.3. The couplings

The effect of the 2^+ and 3^- couplings on the elastic (and fusion) cross sections is very small, as illustrated in figures 16–18. We have verified, in several cases, that the effect on the cross sections of including other states of the quadrupole band in the CC calculations is negligible. As already commented, due to the large binding energy of ^{4}He relative to its neighboring nuclei, the effect of the transfer processes should not be significant either. Thus, although not formally proved, it is reasonable to assume that the effect of any particular coupling on the cross sections should be quite small. In any case, the comparison between data and theoretical predictions shows a behavior quite similar for all systems studied here. This is strong evidence that the failure in describing the elastic process is not related to the coupling to a particular reaction channel since, in this case, it would obviously be dependent on the system. Although the effect of each individual coupling is small, it is still possible that the problem of describing the elastic scattering data set is related to the overall effect of a myriad of couplings to a large number of states (complete inelastic bands, many states of the transfer channels, etc).

To investigate this hypothesis, we performed tests to determine the sensitivity of the elastic cross section to the inelastic couplings of states with high excitation energies. Again, we consider the example of α + ^{208}Pb at $E_{\mathrm{red}} = 6.6$ MeV. We calculated elastic scattering cross sections considering the effect of the coupling to only one target state (2^+ or 3^-—see table 1), as a function of the excitation energy of this state (the excitation energy was considered as a variable parameter). Figure 23 shows the results obtained for four different scattering angles (the quarter-point angle for this angular distribution is $\theta_{1/4} \approx 87^{\mathrm{o}}$). Clearly, the effect of the couplings on the cross section at the forward angles is significantly smaller than that in the backward region. For instance, in the case of the 3^- coupling, for $\theta = 80^{\mathrm{o}}$ the maximum value of the cross section is about 3% larger than that without couplings (dotted lines in figure 23), while for $\theta = 170^{\mathrm{o}}$ the difference reaches about 17%. More important, figure 23 also shows that the forward angles are sensitive to the region of small excitation energies, while the backward angles are mostly affected by states with energies around $E^* \approx 6$ MeV. It is known that the density of the energy levels increases exponentially with the excitation energy (see e.g. [80]). Indeed, there are 7 ^{208}Pb excited states known in the region of $3 \leqslant E^* \leqslant 4$ MeV, approximately 40 with $4 \leqslant E^* \leqslant 5$ MeV, about 120 states at the $5 \leqslant E^* \leqslant 6$ MeV range, and so on. Therefore, even if the effect of the coupling of each particular state is small, the overall effect of hundreds of states with high excitation energies may be quite significant for the elastic scattering cross sections at backward angles.

6. Summary and conclusion

We have analyzed the elastic, inelastic and fusion processes for α-nucleus systems, consistently, within the same context. The purpose here was not to pursue perfect data fits, since this was already done in other works through the adjustment of the OP. We tried to describe the data, without the use of adjustable parameters, by assuming some constraints in the calculations that are based on fundamental grounds. As reported, for α-nucleus systems the couplings to the low-lying excited target states, and probably also those to any other particular direct channel, do not significantly affect the elastic and fusion cross sections. This characteristics is quite important because it allows an unambiguous and quite accurate study of the OP for these systems. We assumed a nuclear interaction that had already been successful for the $\alpha + \alpha$, ^{12}C systems, and we extrapolated the model for several heavier nuclei making use of a realistic systematics of nuclear densities. Furthermore, the parameters of the imaginary potential were also fixed by considering realistic arguments: (1) total absorption of the penetrating wave, (2) no interference on the barrier tunneling, and (3) no effect on the real part of the phase-shift.

The CC predictions are in good agreement with the complete data set, except in the cases of the elastic scattering with very small cross sections. In these cases, the theoretical cross sections are smaller than the data, and systematically larger discrepancies occur for smaller cross sections. We provided a meticulous analysis of the possible sources of this behavior. We have concluded that there is evidence of a slight nuclear transparency in the alpha-nucleus systems. This incomplete absorption of the flux of the elastic channel in frontal collisions ($\ell < \ell_g$) could be related to the effect of inelastic couplings to a very large number of states with high excitation energies. The natural next step of the present study should be provided by quantitative analyzes of the 'extra' elastic cross section and its relation with the $|S_\ell|$ values for other energies and systems. This goal requires considerable effort and will likely be the subject of further works.

Acknowledgments

This work was partially supported by the Fundação de Amparo à Pesquisa do Estado de São Paulo (FAPESP) and the Conselho Nacional de Desenvolvimento Científico e Tecnológico (CNPq). The work at Brookhaven National Laboratory was sponsored by the Office of Nuclear Physics, Office of Science of the US Department of Energy under Contract No. DE-AC02-98CH10886 with Brookhaven Science Associates, LLC.

References

[1] Blocki J, Randrup J, Swiatecki W J and Tsang C F 1977 *Ann. Phys., NY* **105** 427
[2] Brink D M and Stancu F 1978 *Nucl. Phys.* A **299** 321
[3] Satchler G R and Love W G 1979 *Phys. Rep.* **55** 183
[4] Kobos A M, Brown B A, Hodgson P E, Satchler G R and Budzanowski A 1982 *Nucl. Phys.* A **384** 65
[5] Kobos A M, Brown B A, Lindsay R and Satchler G R 1984 *Nucl. Phys.* A **425** 205
[6] Chamon L C, Carlson B V, Gasques L R, Pereira D, De Conti C, Alvarez M A G, Hussein M S, Cândido Ribeiro M A, Rossi E S Jr and Silva C P 2002 *Phys. Rev.* C **66** 014610
[7] Baltz A J, Kauffmann S K, Glendening N D and Pruess K 1978 *Phys. Rev. Lett.* **40** 20
[8] Hussein M S, Rego R A and Bertulani C A 1991 *Phys. Rep.* **201** 279
[9] Nobre G A P, Dietrich F S, Escher J E, Thompson I J and Dupuis M 2010 *Phys. Rev. Lett.* **105** 202502
[10] Koning A and Delaroche J 2003 *Nucl. Phys.* A **713** 231
[11] Mohr P, Kiss G G, Fülöp Z, Galaviz D, Gyürky G and Somorjai E 2013 *At. Data Nucl. Data Tables* **99** 651
[12] Alvarez M A G, Chamon L C, Hussein M S, Pereira D, Gasques L R, Rossi E S Jr and Silva C P 2003 *Nucl. Phys.* A **723** 93
[13] Satchler G R 1983 *Direct Nuclear Reactions* (Oxford: Oxford University Press)
[14] Chamon L C, Gasques L R, Alves L F M, Guimarães V, Descouvemont P, deBoer R J and Wiescher M 2014 *J. Phys. G: Nucl. Part. Phys.* **41** 035101
[15] Avrigeanu M, Obreja A C, Roman F L, Avrigeanu V and von Oertzen W 2009 *At. Data Nucl. Data Tables* **95** 501
[16] Demetriu P, Grama C and Goriely S 2002 *Nucl. Phys.* A **707** 253
[17] Chamon L C, Gasques L R and Carlson B V 2011 *Phys. Rev.* C **84** 044607
[18] De Vries H, De Jager C W and De Vries C 1987 *At. Data Nucl. Data Tables* **36** 495
[19] Carlson B V and Hirata D 2000 *Phys. Rev.* C **62** 054310
[20] Thompson I J 1988 *Comput. Phys. Rep.* **7** 167
[21] Raman S, Nestor C W Jr and Tikkanen P 2001 *At. Data Nucl. Data Tables* **78** 1
[22] Kibedi T and Spear R H 2002 *At. Data Nucl. Data Tables* **80** 35
[23] Chamon L C and Carlson B V 2010 *Nucl. Phys.* A **846** 1
[24] Vaz L C and Alexander J M 1978 *Phys. Rev.* C **18** 2152
[25] Hagino K and Takigawa N 2012 *Prog. Theor. Phys.* **128** 1061
[26] Hill D L and Wheeler J A 1953 *Phys. Rev.* **89** 1102
[27] Oliveira J R B *et al* 2013 *J. Phys. G: Nucl. Part. Phys.* **40** 105101
[28] Trotta M *et al* 2000 *Phys. Rev. Lett.* **84** 2342
[29] Huizenga J R, Vandenbosch R and Warhanek H 1961 *Phys. Rev.* **124** 1964
[30] Viola V E Jr and Sikkeland T 1962 *Phys. Rev.* **128** 767
[31] Limkilde P and Sletten G 1973 *Nucl. Phys.* A **199** 504
[32] Freiesleben H and Huizenga J R 1974 *Nucl. Phys.* A **224** 503
[33] Halász Z, Gyürky G, Farkas J, Fülöp Z, Szücs T and Somorjai E 2012 *Phys. Rev.* C **85** 025804
[34] Barnett A R and Lilley J S 1974 *Phys. Rev.* C **9** 2010
[35] Kelly E L and Segre E 1949 *Phys. Rev.* **75** 999
[36] Remler W J, Wing J, Henderson D J and Huizenga J R 1959 *Phys. Rev.* **114** 154
[37] Rizvi I A, Bhardwaj M K, Ansan M A and Chaubey A K 1990 *Appl. Radiat. Isot.* **41** 215
[38] Hermanne A, Tárkányi F, Takács S, Szücs Z, Shubin Y N and Dityuc A I 2005 *Appl. Radiat. Isot* **63** 1

[39] Lambrecht R M and Mirzadeh S 1985 *Appl. Radiat. Isot.* **36** 443
[40] Lukyanov S M *et al* 2009 *Phys. Lett.* B **670** 321
[41] Wojciechowski H, Medsker L R and Davis R H 1977 *Phys. Rev.* C **16** 1767
[42] Somorjai E *et al* 1998 *Astron. Astrophys.* **333** 1112
[43] Denzler F O, Rosch F and Qaim S M 1995 *Radiochim. Acta* **68** 13
[44] Gyürky Gy *et al* 2006 *Phys. Rev.* C **74** 025805
[45] Rapp W, Dillmann I, Käppeler F, Giesen U, Klein H, Rauscher T, Hentschel D and Hilpp S 2008 *Phys. Rev.* C **78** 025804
[46] Özkan N *et al* 2007 *Phys. Rev.* C **75** 025801
[47] Khulelid D E, Chikhlad V L, Maksimov M Z and Onufriev V G 1965 *Sov. Phys—JETP* **20** 259
[48] Rebeles R A, Hermanne A, Takács S, Tárkányi F, Kovalev S F and Ignatyuk A 2007 *Nucl. Instrum. Methods* B **260** 672
[49] Fülöp Z, Kiss A Z, Somorjai E, Rolfs C E, Trautvetter H P, Rauscher T and Oberhummer H 1996 *Z. Phys.* A **355** 203
[50] Calboreanu A, Salagean O, Pencea C, Zimmer K W and Ciocanel A 1987 *Rev. Roum. Phys.* **32** 725
[51] Qaim S M, Mushtaq A and Uhl M *Phys. Rev.* C **38** 645
[52] Di Pietro A *et al* 2004 *Phys. Rev.* C **69** 044613
[53] Scuderi V *et al* 2011 *Phys. Rev.* C **84** 064604
[54] Gyürky G, Mohr P, Fülöp Z, Halász Z, Kiss G G, Szücs T and Samorjai E 2012 *Phys. Rev.* C **86** 041601
[55] Stelson P H and McGowan F K 1964 *Phys. Rev.* **133** B911
[56] Abu Issa N N, Khrisanfov Yu V, Antropov A E, Zarubin P P, Smirnov A V and Gusev V P 1987 *37 Conf. Nucl. Spectrosc. and Nucl. Struct (Jurmala, USSR)* 353. EXFOR A0337.003
[57] Porile N T 1959 *Phys. Rev.* **115** 939
[58] Ball J B, Fairhall A W and Halpern I 1959 *Phys. Rev.* **114** 305
[59] McGowan F K, Stelson P H and Smith W G 1964 *Phys. Rev.* **133** B907
[60] Morinaga H 1956 *Phys. Rev.* **101** 100
[61] Vlieks A E, Morgan J F and Blatt S L 1974 *Nucl. Phys.* A **224** 492
[62] Barnett A R, Feng D H and Goldfarb L J B 1974 *Phys. Lett.* B **48** 290
[63] Lilley J S, Franey M A and Feng D H 1980 *Nucl. Phys.* A **342** 165
[64] Barnett A R and Phillips W R 1969 *Phys. Rev.* **186** 1205
[65] Baker F T, Scott A and Styles R C 1981 *Nucl. Phys.* A **351** 63
[66] Burnett S M, Baxter A M, Hinds S, Pribac F, Smith R, Spear R H and Fewell M P 1985 *Nucl. Phys.* A **442** 289
[67] Trombik W, Eberhard K A, Hinderer G, Rossner H H, Weidinger A and Eck J S 1974 *Phys. Rev.* C **9** 1813
[68] Palumbo A *et al* 2012 *Phys. Rev.* C **85** 035808
[69] Gasques L R *et al* 2003 *Phys. Rev.* C **67** 024602
[70] Watson B D, Robson D, Tolbert D D and Davis R H 1971 *Phys. Rev.* C **4** 2240
[71] Eisen Y, Abramson E, Engler G, Samuel M, Smilansky U and Vager Z 1974 *Nucl. Phys.* A **236** 327
[72] Miler M, Kleinfeld A M, Bockisch A and Bharuth-Ram K 1981 *Z. Phys.* A **300** 97
[73] Badawy I, Berthier B, Charles P, Dost M, Fernandez B, Gastebois J and Lee S M 1978 *Phys. Rev.* C **17** 978
[74] Tabor S L, Watson B A and Hanna S S 1975 *Phys. Rev.* C **11** 198
[75] Karcz W, Kluska I, Sanok Z, Szmider J, Szymakowski J, Wiktor S and Wolski R 1972 *Acta Phys. Pol.* B **3** 525 (EXFOR F0700.010)
[76] Fülöp Z *et al* 2001 *Phys. Rev.* C **64** 065805
[77] Galaviz D, Fülöp Z, Gyürky G, Máté Z, Mohr P, Rauscher T, Somorjai E and Zilges A 2005 *Phys. Rev.* C **71** 065802
[78] Herman M, Capote R, Carlson B V, Obložinský P, Sin M, Trkov A, Wienke H and Zerkin V 2007 *Nucl. Data Sheets* **108** 2655
[79] Herman M *et al* 2013 EMPIRE-3.2 Malta Modular system for nuclear reaction calculations and nuclear data evaluation *International Atomic Energy Agency and Brookhaven National Laboratory Report* INDC(NDS)-0603, BNL-101378-2013
[80] von Egidy T and Bucurescu D 2005 *Phys. Rev.* C **72** 044311